Optimization of a calibration phantom for quantitative radiography

Cristóbal Martinez*
Department. Bioingeniería e Ingeniería Aeroespacial, Universidad Carlos III de Madrid, Madrid, Spain
Instituto de Investigación Sanitaria Gregorio Marañón, Madrid, Spain

Claudia de Molina*
Department. Bioingeniería e Ingeniería Aeroespacial, Universidad Carlos III de Madrid, Madrid, Spain

Manuel Desco[a)]
Department. Bioingeniería e Ingeniería Aeroespacial, Universidad Carlos III de Madrid, Madrid, Spain
Instituto de Investigación Sanitaria Gregorio Marañón, Madrid, Spain
Centro Nacional de Investigaciones Cardiovasculares Carlos III (CNIC), Madrid, España
Centro de investigación en red en salud mental (CIBERSAM), Madrid, Spain

Mónica Abella[a)]
Department. Bioingeniería e Ingeniería Aeroespacial, Universidad Carlos III de Madrid, Madrid, Spain
Instituto de Investigación Sanitaria Gregorio Marañón, Madrid, Spain
Centro Nacional de Investigaciones Cardiovasculares Carlos III (CNIC), Madrid, España

(Received 27 March 2020; revised 26 October 2020; accepted for publication 20 November 2020; published xx xxxx xxxx)

Objective: Dual energy radiography (DER) makes it possible to obtain separate images for soft tissue and bony structures (tissue maps) based on the acquisition of two radiographs at different source peak-kilovoltage values. Current DER studies are based on the weighted subtraction method, which requires either manual tuning or the use of precomputed tables, or decomposition methods, which make use of a calibration to model soft-tissue and bone components. In this study, we examined in depth the optimum method to perform this calibration.
Methods: We used simulations to optimize the calibration protocol and evaluated the effect of the material and size of a calibration phantom composed of two wedges and its positioning in the system. Evaluated materials were water, PMMA and A-150 as soft-tissue equivalent, and Teflon, B-100 and aluminum as bone equivalent, with sizes from 5 to 30 cm. Each material combination was compared with an ideal phantom composed of soft tissue and bone. Our simulation results enabled us to propose four designs that were tested with the NOVA FA X-ray system with a realistic thorax phantom.
Results: Calibration based on a very simple and inexpensive phantom with no strict requirements in its placement results in appropriate separation of the spine (a common focus in densitometry studies) and the identification of nodules as small as 6 mm, which have been reported to have a low rate of detection in radiography.
Conclusion: The proposed method is completely automatic, avoiding the need for a radiology technician with expert knowledge of the protocol, as is the case in densitometry exams. The method provides real mass thickness values, enabling quantitative planar studies instead of relative comparisons.
 [https://doi.org/10.1002/mp.14638]

Key words: calibration, dual energy, quantitative radiography, x-ray

1. INTRODUCTION

Dual energy radiography (DER) is based on differences in attenuation properties of body tissues for low- and high-energy x-ray photons. This approach makes it possible to obtain separate images for soft tissue and bony structures. Its benefits over conventional radiography have been proven in chest imaging for the following: differentiation between lung nodules and calcified lesions or identification of tracheal and airway abnormalities; determination of fat content to predict metabolic syndrome in abdominal studies[1]; and assessment of bone mineral density and bone mineral content in limb studies.[2,3]

A DER study comprises of acquisition of radiographs at two different source peak-kilovoltage values. In most radiography systems with polychromatic spectra and energy-integrating detectors, these measurements can be modeled as follows:

$$I_{L,H} = \int_{\varepsilon} N_{L,H}(\varepsilon) e^{-\sum_i \int_P \mu_i(\varepsilon) dt} d\varepsilon, \quad (1)$$

where $I_{L,H}$ is the measurement at the detector for the low (L) and high (H) peak-kilovoltage, $N_{L,H}(\varepsilon)$ the number of incident photons at the detector without sample (flood field image) for each energy ϵ, and μ the attenuation coefficient, which can be expressed as:

M P | Journal Code | 14638 | Manuscript No. | WILEY | Dispatch: 14.12.20 | No. of pages: 15 | CE: | PE: Karthick N.

$$\int_P \mu_i(\varepsilon)dt = x_i\frac{\mu_i}{\rho_i}(\varepsilon), x_i = \int_P \rho_i dt, \quad (2)$$

where μ_i/ρ_i, x_i and ρ_i are the mass attenuation coefficients, the mass thickness, and the physical density of material i along the path P followed by the beam. From these acquired data, we can obtain images corresponding to the mass thickness of each tissue, which we refer to as tissue maps throughout the paper. Log-weighted subtraction is a common approach that estimates equivalent tissue maps for soft tissue, x_s, and bone, x_b, by combining the low- and high-energy measurements with two different global weighting parameters for the whole image.[4,5] In Skhumat et al.,[4] the weighting parameters were empirically chosen by requiring the user to select different regions in the image. The user interaction was reduced in Ergun et al.[5] by estimating an initial approximation of the weights based on knowledge of the spectra. The main disadvantage of these approaches is that results depend to a large extent on the expertise of the operator. To completely reduce the interaction of the operator, General Electric (GE)[6,7] used precomputed weights for each combination of peak-kilovoltage, source filtration and the size of the patient. To avoid the use of the precomputed table, GE developed a method[8] to automatically calculate these weights from a ratio image obtained with the low and high peak-kilovoltage acquisitions.

Alternatively, decomposition methods use higher-order models to associate the tissue maps corresponding to soft tissue and bone, x_s and x_b, with the natural logarithm of the measured photons at the detector over the total incident photons, d_L and d_H (second order,[9–13] third order[14–17] or other models such as conic and cubic surface equations[18]):

$$x_s = \sum_{m=0}^{M}\sum_{n=0}^{N} q_{mn} d_L^m d_H^n; \; x_b = \sum_{m=0}^{M}\sum_{n=0}^{N} r_{mn} d_L^m d_H^n \quad (3)$$

$$d_L(t_s,t_b) = Ln\left(I_L/\int N_L(\varepsilon)d\varepsilon\right); \; d_H(t_s,t_b) = Ln\left(I_H/\int N_H(\varepsilon)d\varepsilon\right) \quad (4)$$

where the model parameters q_{mn} and r_{mn} can be obtained from a calibration step by acquiring different known combinations of x_s and x_b at low and high energies, which correspond to d_L and d_H. The equivalent materials used for the calibration need to resemble the attenuation of X-rays by soft tissue and bone for different energies, which can be represented by the *dual-material dependency* with the energy, $DMD(x_s, x_b)$, shown in Fig. 1. $DMD(x_s, x_b)$ is the relation between the thickness of traversed materials and the attenuation produced.

The soft-tissue equivalent materials reported in the literature comprise polymethyl methacrylate (PMMA),[9,10,18] water,[15] and plastic.[11] The most common bone equivalent materials were aluminum[9,11,15,18] and calcium sulfate powder.[10,13] Nevertheless, no previous studies presented a thorough study of the material properties needed to select the optimum substitute materials that best characterize the x-ray system. This calibration can be facilitated by using a calibration phantom with a shape that enables simultaneous measurement of different combinations of soft tissue and bone as found in clinical studies. The literature provides little data on the optimal shape and size of this phantom.

The studies[10,11,18] are based on very-small-step numerical simulations of different thicknesses of ideal materials that are difficult to achieve in a real experiment. In Brody et al.,[15] a phantom formed by two wedges was suggested to simultaneously acquire multiple combinations of the two materials. The estimation of the traversed mass thicknesses [x_s and x_b in Eq. (3)] corresponding to each measurement can be easily obtained in the case of computed tomography (CT) systems by segmenting both materials in the 3D reconstruction of the calibration phantom. Nevertheless, it becomes a more complex process in planar systems owing to the lack of tomographic data. In these scenarios, the traversed thicknesses can be obtained from a simulation of the phantom placed in the system during acquisition, provided complete geometric characterization is available.

In this study, we used simulations to study the optimum design of the calibration phantom in terms of material and size and to evaluate the effect of errors on the estimation of the geometry needed to calculate the traversed mass thicknesses corresponding to each measurement. From the results of the simulation study, we selected four designs and tested them in practice using a NOVA FA X-ray system from SEDECAL (Algete-Madrid, Spain).

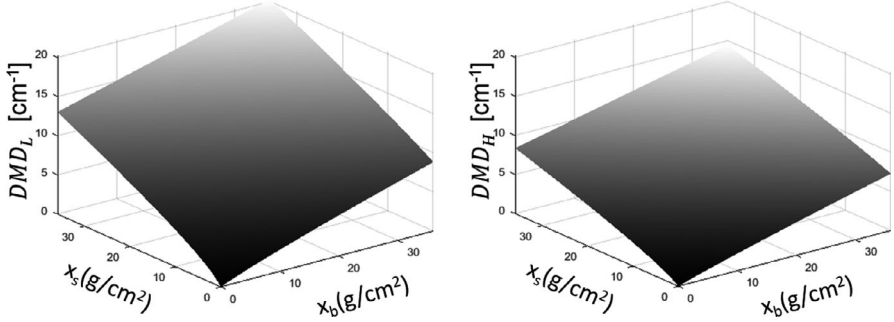

FIG. 1. Dual-material dependency of the system at low (left) and high (right) energies.

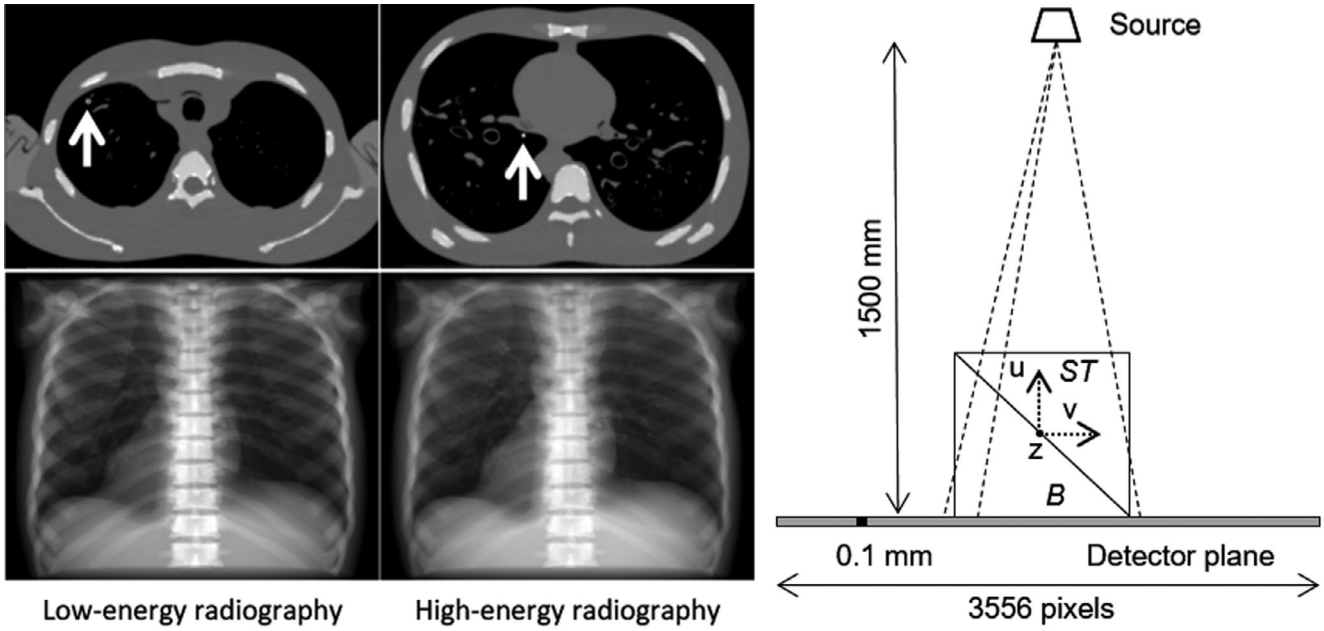

FIG. 2. Left: computed tomography (top), where the white arrows indicate a soft tissue nodule and a calcification, and simulated DER (bottom) of the chest anthropomorphic phantom PBU-60 (Kyoto Kagaku). Right: Geometry used for simulations with the calibration phantom; ST and B refer to the equivalent soft tissue and bone materials, respectively.

2. MATERIALS AND METHODS

2.A. Simulation data: clinical study

Simulations were carried out using FUX-Sim,[19] a simulation framework for x-ray systems. Spektr was used to generate 70 and 140 kVp spectra,[20] and the x-ray attenuation of each material was extracted from National Institute of Standards and Technology (NIST) tables.[21] The detector was modeled as a simple photon-counting device, with a matrix size of 4320 × 3556 pixels and 100 μm pixel size. The source-detector distance was 150 cm.

A chest CT of the anthropomorphic phantom PBU-60 (Kyoto Kagaku) was obtained with a Toshiba Aquilion/LB scanner (voxel size of 0.931 mm × 0.931 mm × 0.5 mm), segmented into soft tissue and bone volumes by thresholding, and converted from Hounsfield units to ideal density values by a linear transformation. This transformation was obtained by measuring the mean value on homogeneous regions of air and soft tissue and assigning them to ideal density values of 0 and between 1 and 1.1 g/cm^3, respectively, as described in Report 44 from the International Commission on Radiation Units and Measurements (ICRU).[22] Resulting bone values were between 1.4 and 2.4 g/cm^3.

We simulated two spherical lesions smaller than 10 mm, which is a size limit reported to show a low rate of detection using conventional chest radiography.[23] One was a nodule (ρ = 1.1 g/cm^3 and diameter = 8 mm) that was placed behind the ribs with the mass attenuation coefficient of the soft tissue (from NIST tables[21]); the other was a calcification (ρ = 1.4 g/cm^3 and diameter = 6 mm) that was placed behind the heart (Fig. 2, left) with the mass attenuation coefficient of the bone (from NIST tables[21]). Neither can be seen in the simulated low- and high-energy radiographs. The ideal tissue maps were calculated by projecting the soft tissue and bone volumes separately and used as the reference images for the dual energy subtraction.

To evaluate the consistency of the model for larger patients (extrapolation for higher thickness of soft tissue), we simulated an obese patient[24] by adding 7 cm of soft tissue to the anthropomorphic phantom with 7 cm of added soft tissue, as shown in Fig. 3.

2.B. Simulation data: calibration study

We simulated a calibration phantom made of two wedges of equivalent soft tissue and bone materials.[12,14,15] The geometry used for the simulations is shown in the right panel of Fig. 2, with the soft-tissue equivalent wedge closer to the x-ray source in order to obtain measurements of only soft tissue (Fig. 2). The workflow followed for the simulation study is summarized in Fig. 4.

2.B.1. Equivalent materials study

We first studied the candidate materials for each tissue in terms of its physical properties, manufacturability, cost, and energy dependency. Table I shows the materials studied for soft-tissue and bone wedges in the phantom; most had previously been proposed in the literature as bone and soft-tissue substitutes. Since it is not possible to have a phantom made of water, we tested a hollow prism of PMMA with a wall thickness of 5.6 mm filled with water (henceforth, "water in PMMA"). Similarly, since the manufacturing of a pure

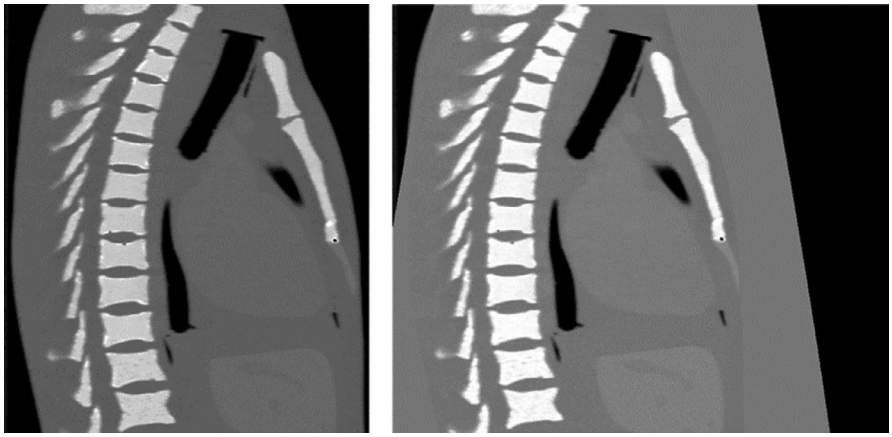

FIG. 3. Sagittal view of the normal computed tomography (left) and the one with extra soft tissue (right).

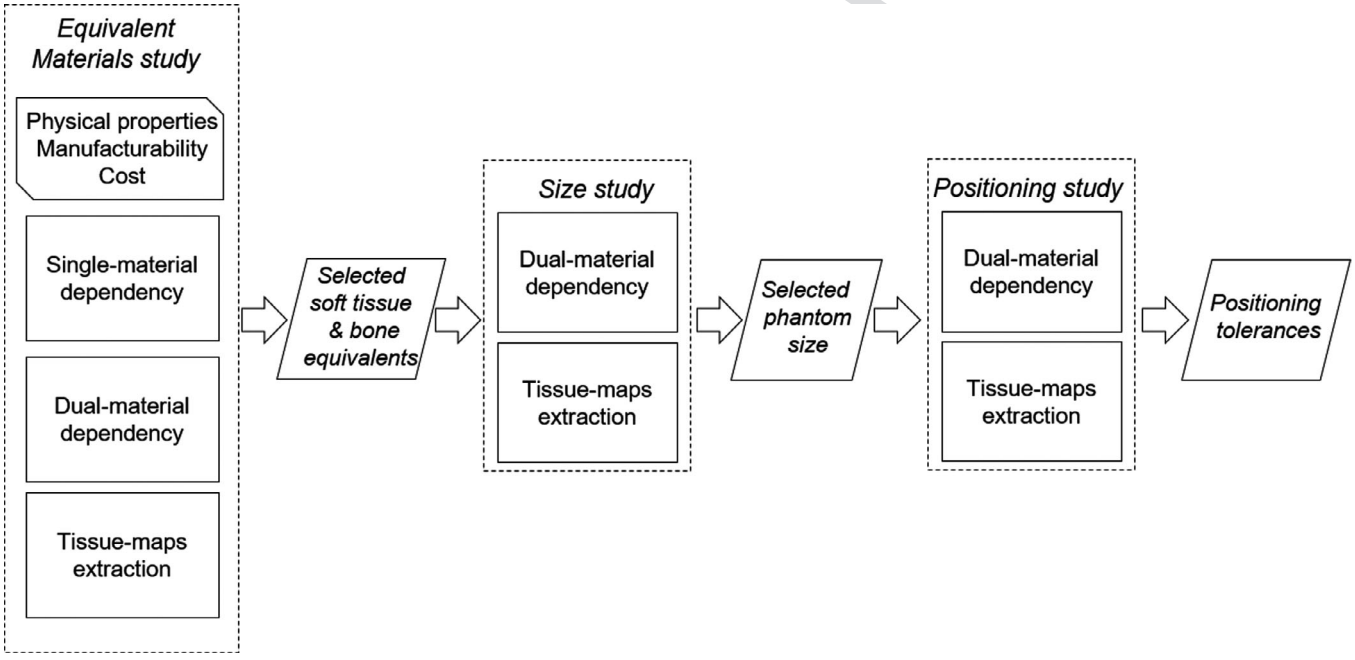

FIG. 4. Steps followed in the simulation study.

aluminum phantom is not possible owing to its low machinability, we evaluated available alloys from the aluminum association with good machinability and few metal impurities and impurities involving metals with a low atomic number. Alloy AL6082 was found to be very similar to pure aluminum (Z = 13), which contains very low concentrations of heavy metals (only iron).

A simulation was run to evaluate each candidate material using a calibration phantom composed of the material evaluated in the corresponding wedge and the ideal material in the other wedge. To study the best candidate material for mimicking soft tissue, we set one wedge of ideal cortical bone (ICRU-44) and made the other wedge of PMMA, water, plastic A-150, and a prism with a wall thickness of 5.6 mm filled with water (water in PMMA). To evaluate candidate materials for mimicking bone, we set one wedge of ideal soft tissue ICRU-44 and tested Teflon, B-100, pure aluminum, and alloy AL6082 in the other wedge. For each simulation, besides evaluating physical density, mean ratio of atomic number-to-mass (Z/A), manufacturability, and cost, we studied the theoretical dependency of total attenuation with the energy. We will refer to the latter as *single-material dependency* of that candidate, $SMD_{L,H}(\mathrm{x_{cand}})$, which is calculated as:

$$SMD_L(x_{cand}) = Ln\left(\frac{\int N_L(\varepsilon)e^{-x_{cand}m_{cand}(\varepsilon)}d\varepsilon}{\int N_L(\varepsilon)d\varepsilon}\right),$$
$$SMD_H(x_{cand}) = Ln\left(\frac{\int N_H(\varepsilon)e^{-x_{cand}m_{cand}(\varepsilon)}d\varepsilon}{\int N_H(\varepsilon)d\varepsilon}\right) \quad (5)$$

Values of $SMD_{L,H}(\mathrm{x_{cand}})$ were obtained for mass thickness values up to 27 and 12 g/cm^2 for soft tissue and bone, respectively (these limits were obtained from a standard chest study,[4] in steps of 0.2 g/cm^2. Single-material dependency can be modeled with a perfect fit ($R^2 = 1$) using a second and a

fourth order power series for the log measurements of soft tissue and bone, respectively. We calculated the *single-material dependency error* (*SME*) as follows:

TABLE I. Materials evaluated for soft tissue and bone substitutes.

	Soft tissue equivalent				
Material	Ideal soft tissue	Water	PMMA	A-150	Water in PMMA
Density (g/cm^3)[a]	1.06	1	1.18	1.127	NA
Z/A ratio	0.55	0.555	0.539	0.549	NA
Machinability	NA	Difficult	Easy	Difficult	Easy
Cost	NA	Low	Low	High	Low

	Bone equivalent				
Material	Ideal cortical bone	Teflon	B-100	Pure Al	Al6082
Density (g/cm^3)[a]	1.92	2.25	1.45	2.7	2.7
Z/A ratio	0.515	0.48	0.527	0.485	*
Machinability	n/a	Easy	Easy	Impossible	Easy
Cost	n/a	Low	High	Low	Low

[a]Values extracted from NIST.[21]

$$SME = |SMD_{L,H}(x_{cand}) - SMD_{L,H}(x_{ideal})| \quad (6)$$

where x_{cand} and x_{ideal} correspond to the mass thicknesses of the candidate and ideal materials, respectively.

Additionally, we obtained the dual-material dependency, $DMD(x_s, x_b)$, by simulating the volume corresponding to each material (size 280, 0.07 mm isotropic voxel) with density values corresponding to the soft-tissue and bone materials tested at each experiment. The traversed mass thicknesses [x_s and x_b in Eq. (3)] were obtained by projecting these volumes and used to simulate the 2D low- and high-energy log measurements resulting from application of Eq. (4). The whole process is depicted in Fig. 5.

Taking into account the order of the power series with the best fit for the single-material dependency of ideal soft tissue and bone (see above), the dual-material dependency of the system was fitted, using a least-square method, with a power series of M = 2 and N = 4 orders with 12 coefficients:

$$DMD(x_s, x_b) = \sum_{m=0}^{M} \sum_{n=0}^{N} a_{mn} x_s^m x_b^n \quad (7)$$

The dual-material dependency *error* (*DME*), was calculated as the percentage of the root-mean-squared error between the values of $DMD(x_s, x_b)$ obtained with the candidate materials and those obtained with the ideal phantom:

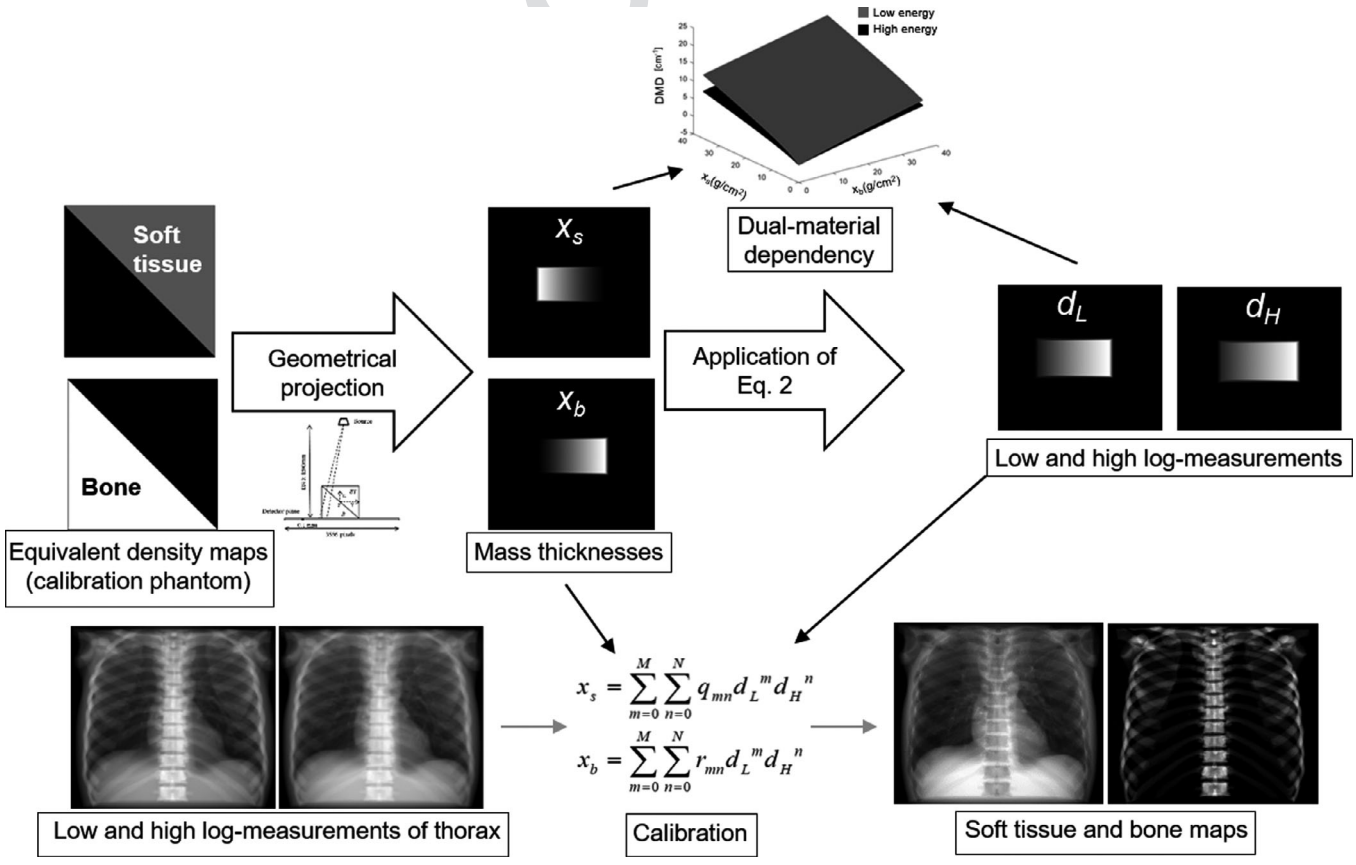

FIG. 5. Workflow of the simulation study.

$$DME(\%) = \frac{\sqrt{\frac{1}{n}\sum_{i=1}^{n}\left(DMD(x_{(s_{cand})},x_{(b_{cand})}) - DMD(x_{(s_{ideal})},x_{(b_{ideal})})\right)^2}}{\frac{1}{n}\sum_{i=1}^{n}\left(DMD(x_{(s_{ideal})},x_{(b_{ideal})})\right)} \times 100 \quad (8)$$

Dual-material dependency, $DMD(x_s, x_b)$, was calculated for the same mass thickness range and steps as those used for single-material dependency. Finally, the calibration parameters q_{mn} and r_{mn} in Eq. (3) were obtained using the mass thickness combinations and the corresponding log measurements, as shown in Fig. 5. Since we expect a relation between mass thicknesses and log measurements equivalent to that of the dual-material dependency, we used the same order power series (M = 2 and N = 4). We then used this calibration to obtain the tissue maps on the simulated DER chest study of the anthropomorphic phantom PBU-60 (Kyoto Kagaku). The quality of the tissue maps was assessed in terms of the *tissue-maps error* (*TME*), which was calculated as the difference between ideal tissue maps and the tissue maps obtained with the tested candidate materials:

$$TME(\%) = \frac{\sqrt{\frac{1}{n}\sum_{i=1}^{n}\left(x_{s_{cand},b_{cand}} - x_{s_{ideal},b_{ideal}}\right)^2}}{\left(\frac{1}{n}\sum_{i=1}^{n} x_{s_{ideal},b_{ideal}}\right)} \times 100 \quad (9)$$

2.B.2. Size study

Considering the previous results for each material, we selected the optimum pair of soft tissue and bone equivalent materials and performed simulations with five phantom sizes.

To study the optimum size for sufficient coverage of mass thickness combinations of soft tissue and bone, we simulated five wedge phantoms made of the optimum materials found in the previous section. Simulations followed the geometry in Fig. 2, right for phantom sizes of 50, 100, 150, 200, and 250 mm, with a voxel size of 0.07 mm.

As the amount of bone present in the human body is smaller than that of soft tissue, we then evaluated the optimum soft-tissue equivalent material in combination with different sizes of the bone equivalent material.

2.B.3. Positioning study

Finally, we evaluated the impact of errors in the estimation of the acquisition geometry along the *u*- and *v*-axes (Fig. 2, right) in both *DME* and *TME* values. The effect of *z*-axis error was not considered, since the phantom does not change along that axis. We carried out ten experiments simulating errors of 1, 2, 3, 4, and 5 mm along each axis using a phantom measuring 150 mm (voxel size of 0.07 mm) and made of the optimum materials found previously.

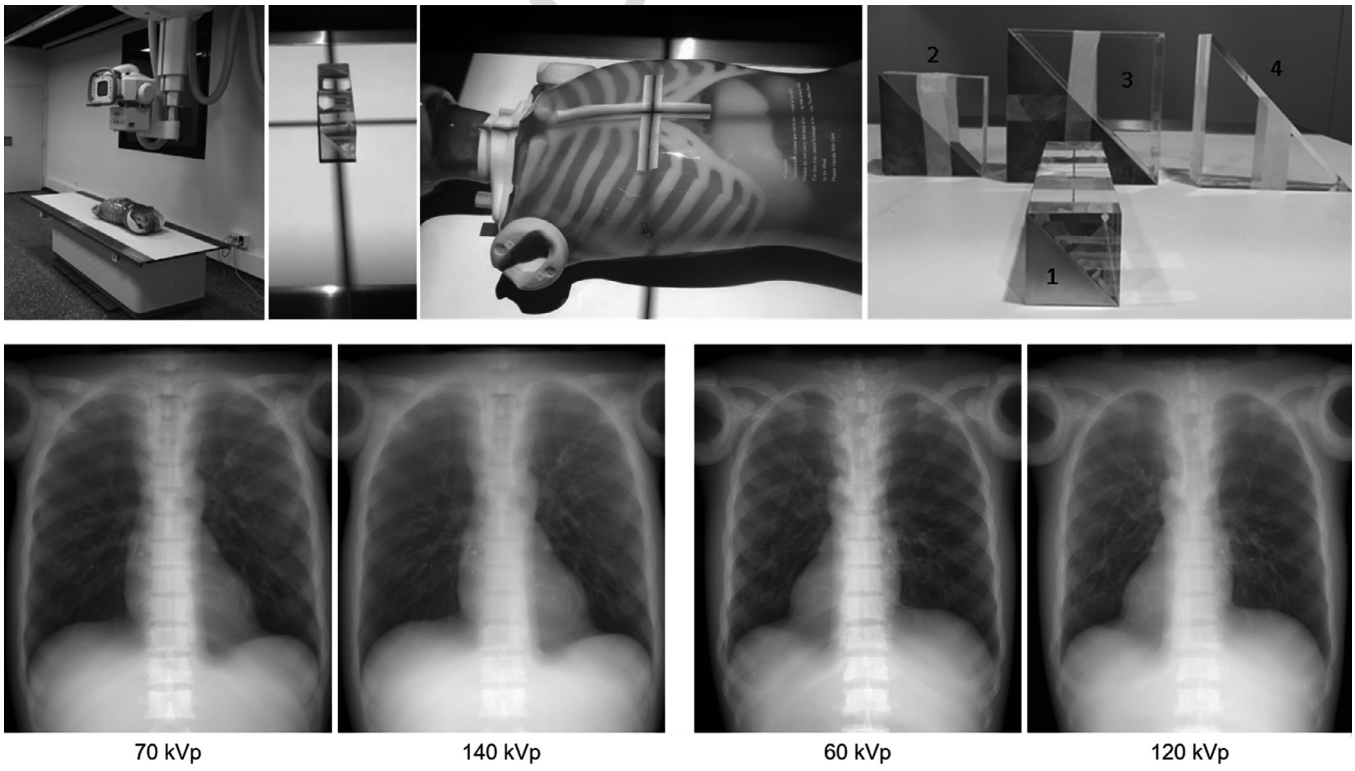

FIG. 6. Top, from left to right: NOVA FA system from SEDECAL, phantom centered with the laser pointer, PBU-60 phantom prepared to acquire low-energy and high-energy in Protocol 1 and dual energy calibration phantoms evaluated. PMMA-AL6082 phantoms with sizes 50 × 50 × 200 mm (a), 100 × 100 × 50 mm (b), 150 × 150 × 50 mm (c), and water in a 3-mm case, together with AL6082 measuring 150 × 150 × 50 mm (d). Bottom: Acquisition pair for Protocol 1 (left) and 2 (right).

2.C. Real data: Clinical study

The study on real data was performed using a clinical NOVA FA system from SEDECAL (Fig. 6). The images were acquired with a flat panel detector (Perkin Elmer XRpad 4320 × 3556) with a pixel size of 100 μm and an anti-scatter grid with a grid ratio of 10:1. The source parameters were 60 and 70 kVp for low-energy acquisitions and 120 and 140 kVp for high-energy acquisitions; the mAs was selected using the automatic exposure control (AEC) of the system to ensure similar signal-to-noise ratio in all images.

We acquired two protocols of dual energy chest studies of the PBU-60 phantom (Kyoto Kagaku). The first one employed a source voltage of 70 and 140 kVp and an exposure of 10.24 and 1.5 mAs, respectively, chosen using the AEC cell located in the spine. The chest phantom was placed in the anterior-posterior position with a source to image distance (SID) of 100 cm (Fig. 6). The second one employed a source voltage of 60 and 120 kVp and an exposure of 12.5 and 0.8 mAs, respectively, using the AEC cell located in the lungs. The phantom was placed in posterior-anterior position with a SID of 150 cm (Table II). Projection images were filtered using a 2D Gaussian smoothing kernel with a standard deviation of 2 pixels (0.2 mm) to reduce the Moiré effect caused by the anti-scatter grid.

TABLE II. Acquisition protocols for evaluation in real data.

Protocol	Source voltages	Exposures	AEC location	SID	Patient position
1	70/ 140 kVp	10.24/ 1.5 mAs	Spine	100 cm	Anterior–Posterior
2	60/ 120 kVp	12.5/ 0.8 mAs	Lungs	150 cm	Posterior–Anterior

2.D. Real data: DE calibration

We tested the calibration phantoms constructed (Fig. 6, top right): PMMA-AL6082 phantoms with sizes 50 × 50 × 200 mm (1), 100 × 100 × 50 mm (2), 150 × 150 × 50 mm (3), and water in a 3-mm case, together with AL6082 measuring 150 × 150 × 50 mm (4).

Low- and high-energy projections were obtained with the phantom placed approximately in the center guided by the cross-hair formed by the light beam of the collimator and the positioning laser pointer (Fig. 6, top center).

To obtain the thicknesses traversed for each point in the projection, we created two digital volumes corresponding to the soft-tissue and bone wedges with an isotropic voxel size of 0.1 mm and projected them assuming that the phantom was located in the center along the *x*- and *z*-axis. To compensate errors due to the mechanical tolerance of the system, the position along the *y-axis* was calibrated by acquiring three different radiographs at detector to source distances of 50, 75, and 100 cm from an aluminum sheet with a hole measuring 51.5 mm in diameter placed on top of the bed. The magnification calculated at the three distances was used to estimate the distance between the bed and the detector (as the average of the three values obtained).

The horizontal and vertical position of the phantom (*v*-axis and *z*-axis in Fig. 2, right) was refined by registering the projection data using a rigid transformation. The result of this process corresponds to the estimated soft tissue (x_s) and bone mass thicknesses (x_b). To reduce noise, the acquired data were fitted to a power series with M = 2 and N = 4. Calibration parameters were obtained using soft tissue and bone values constrained to the maximum mass thicknesses found in a clinical study (27 and 12 g/cm^2, respectively).

Figure 7 shows the workflow of the process.

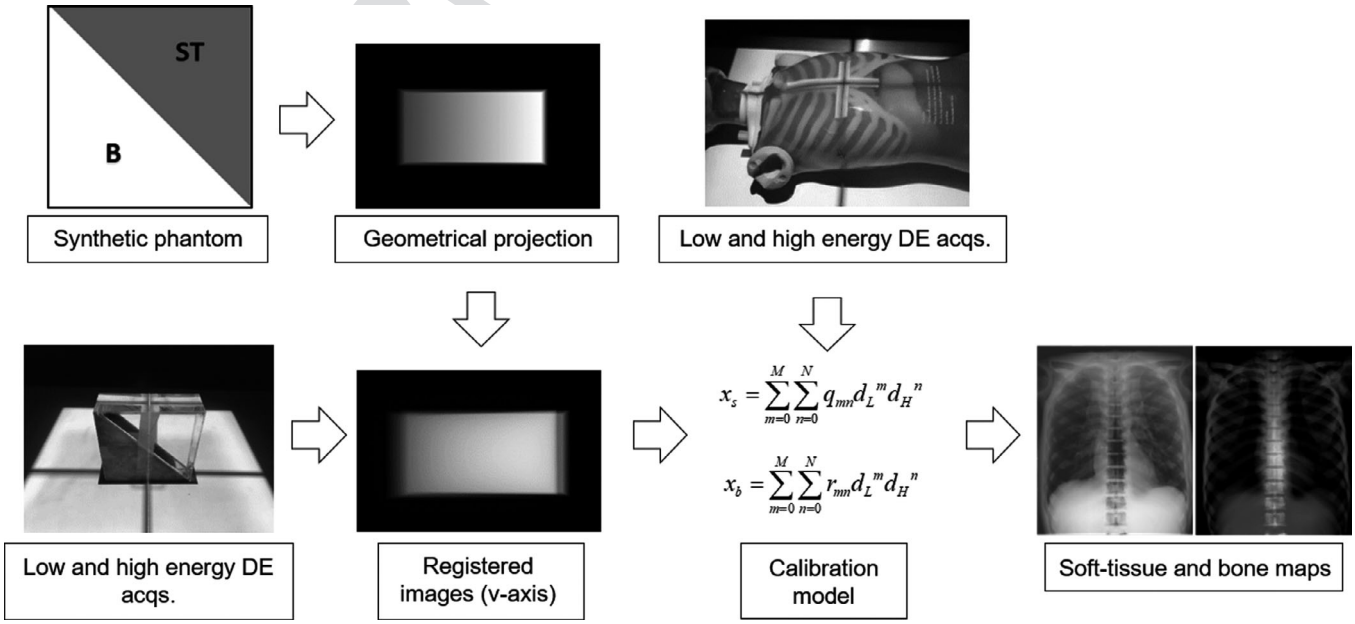

FIG. 7. Workflow of the process.

3. RESULTS

3.A. Simulation study

3.A.1. Equivalent material study

Regarding the soft-tissue equivalent material, all candidates had a relative difference with ideal soft tissue below 12% in density and below 2% in Z/A ratio. The smallest difference in terms of density and Z/A ratio was observed for water and plastic A-150 (Table I).

Figure 8 shows the *SME* corresponding to different mass thicknesses for the case of the low-energy spectrum, which resulted in higher errors. We obtained higher *SME* for PMMA, increasing proportionally to the amount of traversed material, while the smallest *SME* was observed for water. This behavior is also reflected in the *DME*, where water had a *DME* below 0.5%, followed by water in PMMA (0.69%) and Plastic A-150 (below 1%).

Right panel of Fig. 8 shows the results for the tissue maps. All candidate materials led to soft-tissue maps with *TME* under 6%; bone maps present higher error, especially for PMMA with a TME of 51%. The calcification located behind the heart is clearly visible in all four cases. The contrast, measured as the ratio between the mean value in the nodule and the mean value in the background, resulted in a lower value (1.3) in the map obtained with the PMMA phantom than in that obtained with plastic A-150 (2.06), water (2.99), and water in PMMA (1.84). Similarly, the soft tissue in the stomach area was not completely removed with the solid PMMA phantom [Fig. 8(f)]. These results indicate that water would be the optimum material for soft tissue equivalent. A realistic option is the hollow PMMA prism filled with water, which provides similar results, but entails practical issues, such as the need to avoid bubble formation during filling, possible evaporation over time, and waterproofness.

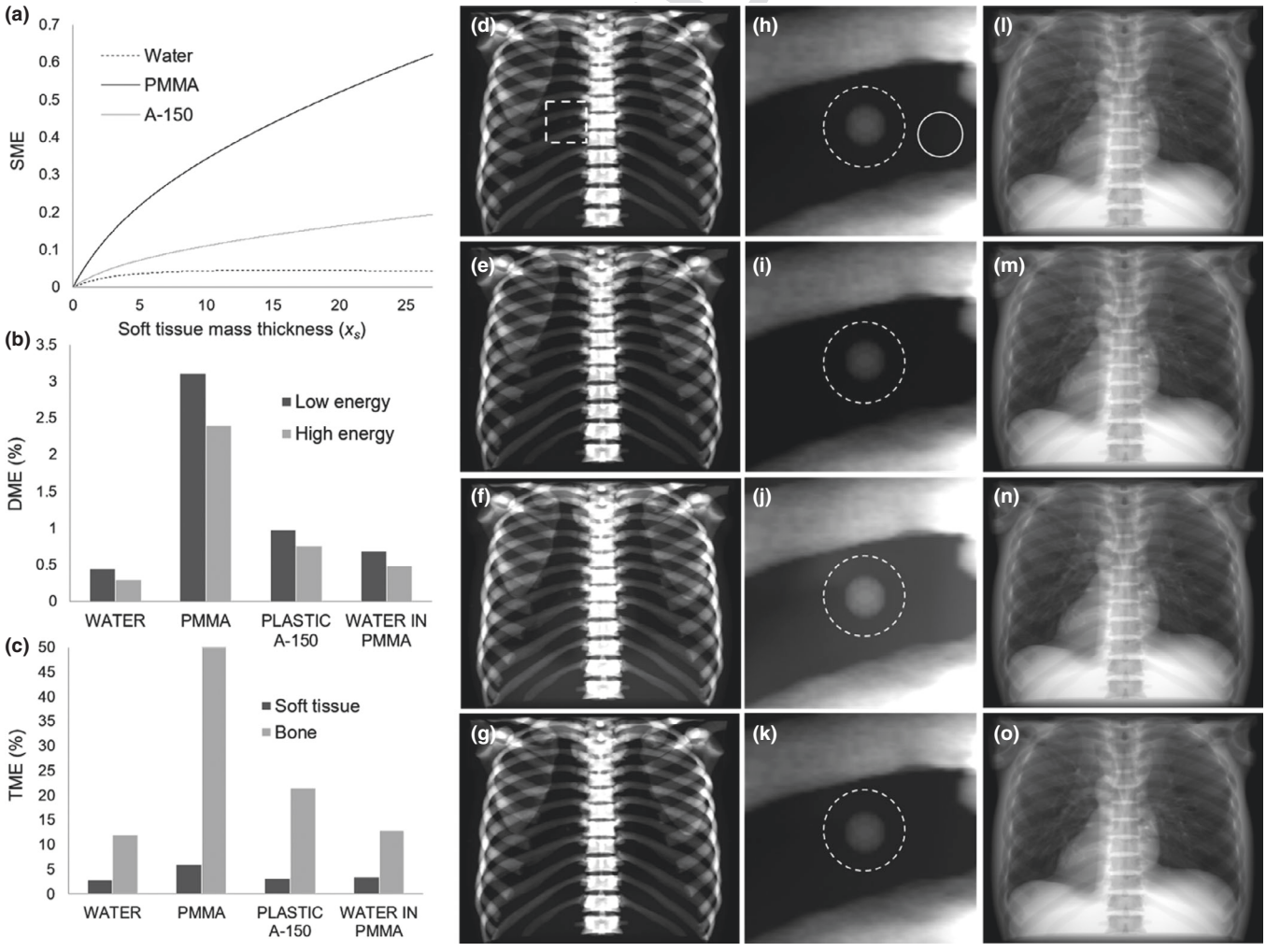

FIG. 8. Single-material error (SME) (a), dual-material dependency error (DME) (b), tissue map error (TME) (c) for all soft tissue candidate materials. Bone maps obtained with the different candidate materials, namely, plastic A-150 (d), water (e), PMMA (f), and water in PMMA (g), with the same window width and level. Zoom of the area within the dashed square with a dashed line shown in (a) for the four cases (h–k). Solid-line circle in the (h) image indicates the area used as background for the calculation of the contrast. Dashed-line circles indicate the calcification in each image. Soft-tissue maps obtained with the different candidate materials (l–o). Same window width and level for bone and soft-tissue maps respectively.

In the case of solid materials, plastic A-150 is the first candidate. Within solids, this option has a physical density and Z/A ratio that are closer to soft tissue than the other candidates. In addition, the *SME*, *DME*, and *TME* are lower. However, plastic A-150 is mostly composed of carbon, which complicates its structural integrity during machinability, and of nylon and polyethylene, which have very different melting temperatures. This makes its construction very difficult and expensive and requires specialized companies.[25,26] Although PMMA presents high values for *SME*, *DME*, and *TME* compared with the other candidates, these errors mainly affect the stomach area of the bone map. However, PMMA enabled correct identification of the calcification [Fig. 8(j)].

Table I shows that all candidates are similar to ideal bone regarding Z/A. The density of Teflon and B-100 is closest to that of ideal bone, with relative differences of 17% and 24%, respectively, compared with aluminum, where the difference is 40%. However, in Fig. 9(a) we can see that Teflon presents the highest *SME*: 1300 times that of the aluminum alloy and increasing proportionally with the amount of traversed tissue. The phantom made of alloy AL6082 shows a clear independence of the *SME* with the traversed tissue, which ensures low error for large amounts of traversed bone. Regarding *DME*, alloy AL6082 presents the smallest error (lower than 1.5%) for the low and high-energy spectrum, while the highest error was obtained with Teflon (25%). Regarding the two tissue maps, higher *TME* values were obtained for bone. Compared with the other materials, AL6082 presented the lowest error: 2% for the soft-tissue map and 7% for the bone map.

The soft-tissue map enabled differentiation of the soft-tissue nodule behind the rib, with all candidates except for Teflon [Fig. 9(i)].

Quantitatively, alloy AL6082 presents the best results and, together with its good machinability, availability, and cost (around 2 euros/kg), makes it an appropriate option for substituting cortical bone during calibration.

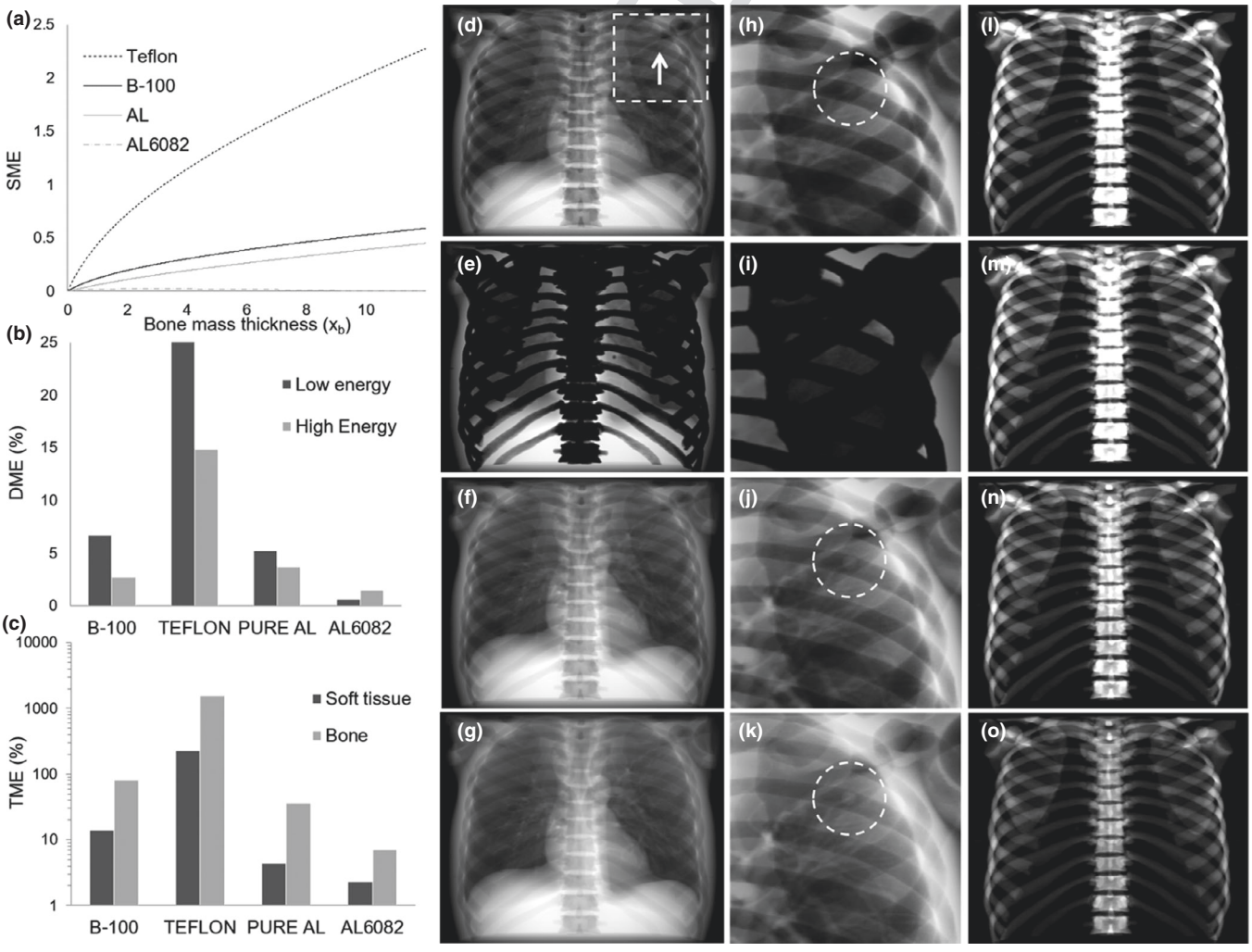

FIG. 9. Single-material error (SME) (a), dual-material dependency error (DME) (b), and tissue map error (TME) (c) for all bone candidate materials. Soft-tissue maps obtained with plastic B-100 (d), Teflon (e), pure aluminum (f), and AL6082 (g), at the same window width and level. Zoomed image of the area within the dashed square highlighted using a dashed line shown in (d) for the four cases (h–k). Dashed circles indicate the location of the soft-tissue nodule. Bone maps obtained with the different candidate materials (l–o). Same window width and level for bone and soft-tissue maps respectively.

3.A.2. Size study

Plots of the mass thickness combinations obtained with the different phantoms (Fig. 10 top) show a lack of values corresponding to small amounts of soft tissue and large amounts of bone, which increase with the phantom size. Nevertheless, the missing data would not be present in a standard chest study, as can be seen in the case of the anthropomorphic phantom PBU. Central panel of Fig. 10 shows that *DME* decreases to 3% for the phantom size of 150 mm and remains constant for larger phantoms. The effect in the tissue maps (measured using *TME*) follows a similar pattern. From these results, we can conclude that a phantom size of 150 mm is sufficiently large for appropriate calibration, with larger phantoms not resulting in lower *DME* or *TME* values. The soft tissue and bone maps obtained with the 50-mm and 150-mm phantoms are shown in Fig. 10, bottom.

Figures 10 and 11 show the results for the optimum wedged size for water in PMMA (in 250 mm) combined with different sizes of AL6082.

Figure 12 shows, as a second iteration, the results for the combination of the optimum AL6082 size (100 mm) and different sizes of water in PMMA (Fig. 12). The optimum water in PMMA phantom size was 300 mm, resulting in a TME of 2.5% and 9.6 % for soft-tissue and bone maps.

Figure 13 shows a proper separation of the soft-tissue and bone maps for the large anthropomorphic phantom case, with similar error values than those for the thinner one (TME of

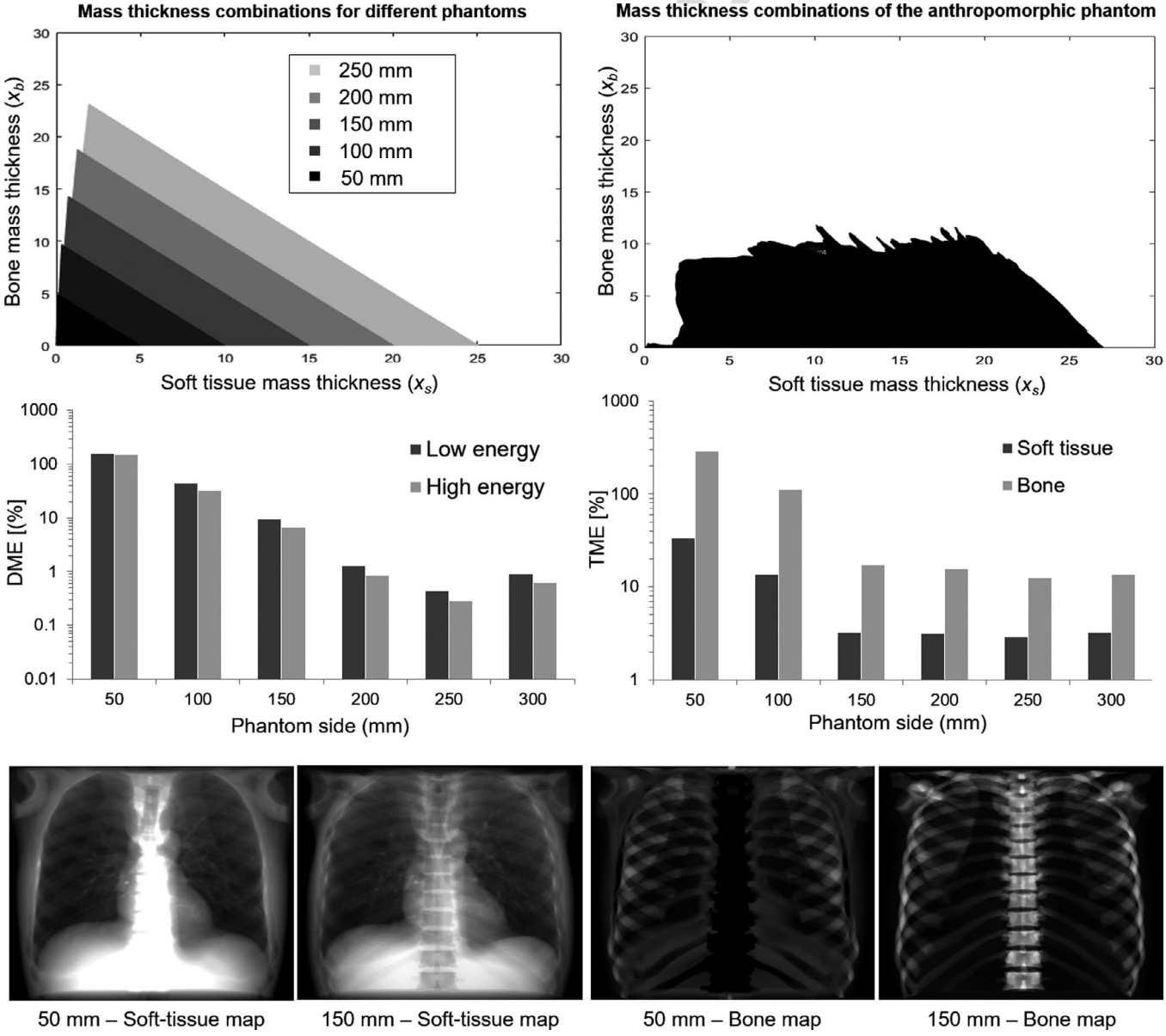

FIG. 10. Top: Thickness combinations of soft tissue and bone provided with the different phantom sizes (left) and obtained with the anthropomorphic thorax phantom (right). Center: dual-material dependency error and tissue-maps error (logarithmic scale) between the ideal and different phantom sides. Bottom: Soft tissue and bone maps obtained with the 50-mm and 150-mm phantoms composed by Water in PMMA and AL6082. Same window width and level for bone and soft-tissue maps respectively.

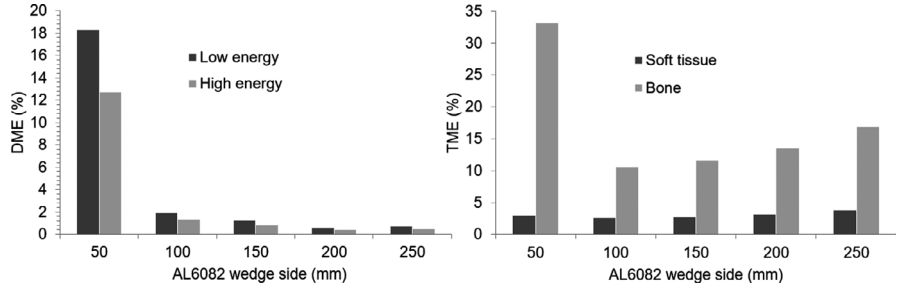

FIG. 11. Dual-material dependency error (left) and tissue-maps error (right) between the ideal and different phantom sides of aluminum 6082 fixing the water in PMMA wedge in 250 mm.

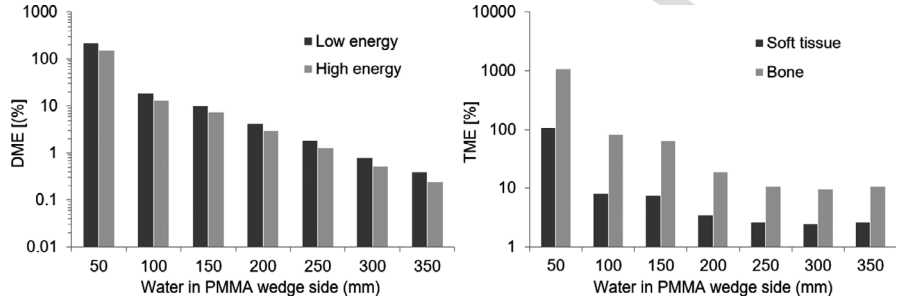

FIG. 12. Dual-material dependency error (left) and tissue-maps error (right) between the ideal and different phantom sides of water in PMMA fixing the aluminum wedge in 100 mm.

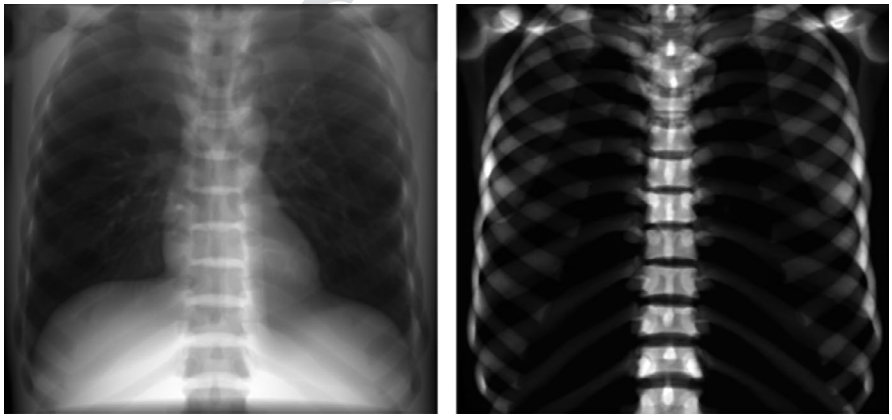

FIG. 13. Soft tissue (left) and bone (right) maps for the anthropomorphic phantom with 7 cm extra of soft tissue.

2.5% and 14.5% for soft-tissue and bone maps respectively), using the optimum phantom.

3.A.3. Positioning study

Finally, regarding phantom positioning, Fig. 14, left shows that errors along the *u* axis do not affect *DME* or *TME* values and for errors along the *v*-axis, *DME* increases linearly, with only the bone map affected. *v*-axis errors larger than 4 mm result in incomplete subtraction of ribs and spine from the soft-tissue map and contrast reduction that hinders the identification of the small lesions (Fig. 14, top right). Errors of about 1 mm along the *v*-axis result in an incomplete subtraction of the abdomen in the bone map (Fig. 14, bottom right).

3.B. Real data

Figure 15 shows the soft-tissue and bone maps obtained with Protocol 1 when the four manufactured calibration phantoms were used on the NOVA FA system. The best separation was obtained with the two largest phantoms (150 mm). We can see better subtraction of the spine when using the Water in PMMA-Al6082 phantom, matching the simulation results.

Figure 16 shows the soft-tissue and bone maps of Protocol 2 with a calibration performed with the 150 mm Water in PMMA-Al6082 phantom. Although part of the stomach appears in the bone map, we can see a good separation of the spine and the ribs.

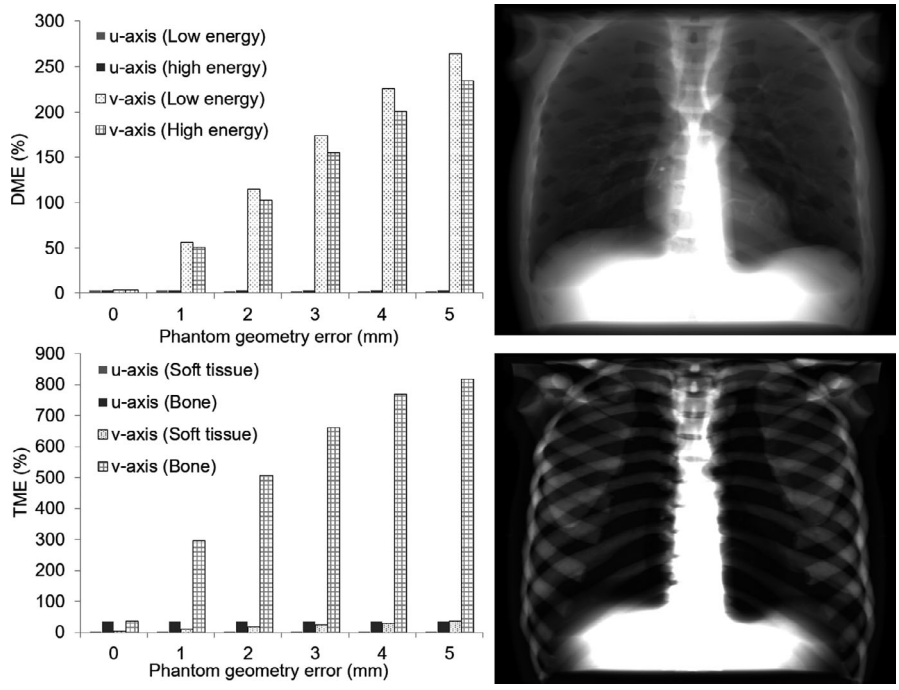

FIG. 14. Left: Dual-material dependency error (left) and tissue-maps error (right) for different geometry errors along the u- and v-axes. Right: Soft-tissue map (top) and bone map (bottom) obtained with 4 and 1 mm of error along the v-axis, respectively. Same window width and level in the images.

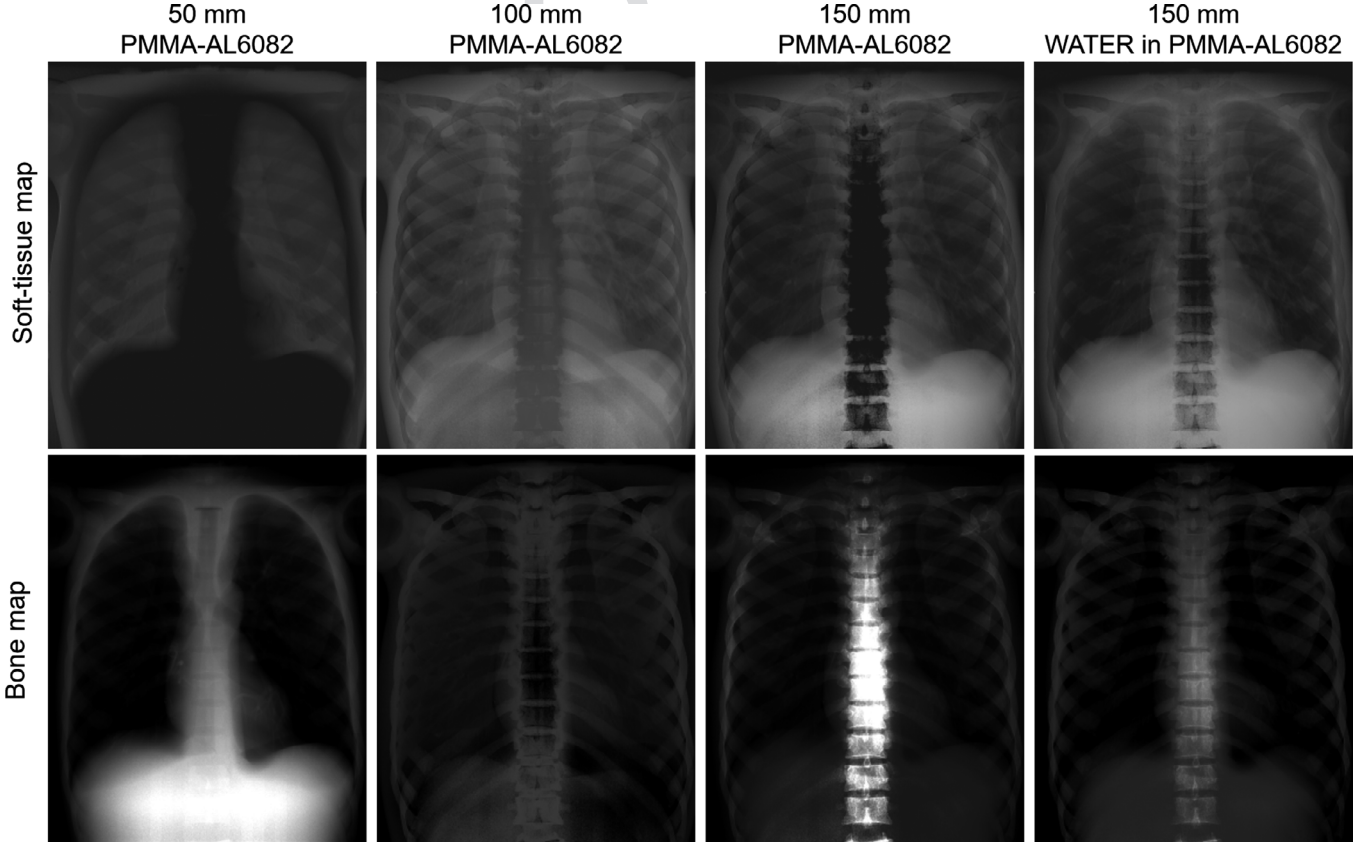

FIG. 15. Soft tissue (top) and bone (bottom) maps obtained in the real system at 100 cm of SID corresponding to the four phantoms evaluated. From left to right: maps obtained with phantoms 1, 2, 3, and 4. Soft tissue and bone maps are shown with the same window-level.

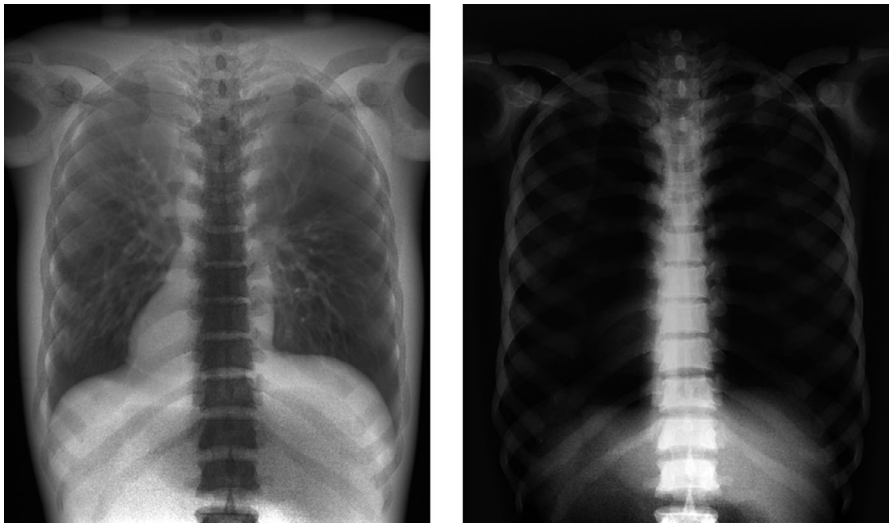

FIG. 16. Soft-tissue (left) and bone (right) maps obtained in the real system at 150 cm of SID corresponding to the 150 mm Water in PMMA-Al6082 phantom.

4. DISCUSSION AND CONCLUSION

We present a comprehensive study of the design of an optimum calibration phantom for DER using both realistic simulations and real data acquired with an X-ray system using an anti-scatter grid. Previous works either studied the recovery of true mass thickness values with simple phantoms giving only numerical results[11,13,17,18] or focused on tissue separation with no error measurements for quantitative purposes.[12,15] Here we present the influence of phantom size and positioning errors on the separation of the soft-tissue and bone maps, both on simulations and real data, using two acquisition protocols with similar characteristics to those of densitometry and chest exams.

Simulations were done with an ideal model in the detector, ignoring the integrating behavior. Nevertheless, the results on data showed similar performance, indicating that this effect does not hinder the separation.

The quantitative study has been performed using an anthropomorphic phantom, which provides more realistic combinations of traversed tissues, instead of the simple phantoms used in previous works.[9,11,13,18] Evaluation was done on an average sized patient and in an obese patient, resulting in a good separation of the tissues in both cases. Thus, the method can be reasonably expected to work with patients of different sizes.

The results of the simulation study showed that energy dependency is essential when choosing equivalent materials. This has a greater impact on the quality of the results than the physical density. For all the materials tested, higher errors were obtained for the low-energy spectrum, owing to the larger differences in the mass attenuation coefficients at low energies. This resulted in errors in the soft-tissue map when nonideal bone materials were tested and vice versa. As a soft-tissue equivalent, water significantly outperformed the remaining candidate materials, with errors below 0.5% in energy characterization and 12% in the tissue maps obtained. We showed that adding the necessary case of PMMA increases errors up to 0.69% and 12%, respectively, although the maps are visually similar. However, it should be taken into account that water-based phantoms require waterproofness and absence of bubble formation, which are not problematic when the least expensive solid material, PMMA, is used. The results with solid PMMA also showed good visual identification of the lesions but no quantitative values (*TME* of 51%).

Teflon, which is widely used as a bone equivalent,[27] did not prove to be optimal for DER, showing incorrect values in the tissue maps obtained. As a bone equivalent, Teflon presented the highest error in energy characterization, that is, 1300 times higher than the alloy AL6082. The latter showed the lowest errors both in energy dependency and in tissue maps (7.2%). This work only explores inexpensive and easily accessible materials; further work will explore the use of more sophisticated materials that may better emulate the x-ray attenuation of soft tissue and bone as those proposed in the literature[13,28–31] or provided by companies as Kyoto Kagaku Company LTD (Japan), Sun Nuclear Corporation or Computerized Imaging Reference Systems, Inc.

We found that a model using a polynomial of second order for the soft tissue and fourth order for the bone resulted in the best tissue separation. However, it would be interesting to carry out a thorough study of other models, such as the ones proposed by Lehman et al.[9] On the other hand, the two-material model simplification may hinder achieving more accurate mass thickness values. FitzGerald et al.[32] suggested that soft tissue could be further divided into two subclasses: (a) adipose tissue and (b) muscle, blood and organs, although the benefits of adding the different soft-tissue classes in dual energy studies is yet to be explored.

Regarding the phantom size, a length of 150 mm was sufficient to yield a good visual separation of the tissues. Nevertheless, the method aims to provide real mass thickness values for each tissue to enable quantitative studies. The phantom composed of 300 mm of water in PMMA and 100 mm of AL6082 resulted in an error lower than 10% for both soft-tissue and bone maps.

The positioning study of the phantom showed almost no effect of errors along the u-axis. As for the v-axis, errors below 4 mm do not affect the soft-tissue maps. Higher sensitivity was found for the bone map, where the abdomen was not properly subtracted, with error values higher than 1 mm, although the calcification remained visible. Following our experimental protocol, which includes geometric calibration and registration, we can expect lower errors in both axes.

Results showed appropriate separation of the spine in the bone map, which is a common focus in densitometry studies, as well as identification of small calcifications or nodules as small as 6 mm, which are reported to have a low rate of detection. As observed in the simulation results, the abdomen was not completely removed from the bone map. Nevertheless, the clinical impact of this problem might not be important in chest imaging, since it does not hinder visualization of the lung when evaluating ground glass opacity or lung nodules. We found an over subtraction of the ribs and the spine in the soft-tissue map, compared to clinical studies. This might be due to the fact that the bone of the anthropomorphic phantom is made of a material that mimics cortical bone while bone of real patients contains cortical bone in the surface and trabecular bone inside, with lower attenuation coefficient value.

The complete protocol for incorporating quantitative dual energy capabilities is completely automatic, based on a preliminary calibration with a very simple and low-cost phantom with no strict placement requirements. This avoids the need for a radiology technician with expert knowledge of the protocol or the use of precomputed tables as in the weighting subtraction method. The method provides real mass thickness values, enabling quantitative planar studies instead of relative comparisons.

ACKNOWLEDGMENT

This work was supported by Ministerio de Ciencia, Innovación y Universidades, Agencia Estatal de Investigación, projects "DPI2016-79075-R - AEI/FEDER, UE ", Instituto de Salud Carlos III, project "DTS17/00122", co funded by European Regional Development Fund (ERDF), "A way of making Europe" Europe". Also partially funded by project "DEEPCT-CM-UC3M", funded by the call "Programa de apoyo a la realización de proyectos interdisciplinares de I + D para jóvenes investigadores de la Universidad Carlos III de Madrid 2019-2020 en el marco del Convenio Plurianual Comunidad de Madrid - Universidad Carlos III de Madrid"). The CNIC is supported by the Ministerio de Ciencia, Innovación y Universidades and the Pro CNIC Foundation, and is a Severo Ochoa Center of Excellence ("SEV-2015-0505"). We thank Carlos Cobos Pérez for his help with the manufacturing of the calibration phantoms.

CONFLICT OF INTEREST

The authors have no conflict to disclose.

DATA AVAILABILITY STATEMENT

All relevant data are available from the Zenodo database, under the https://doi.org/10.5281/zenodo.1413426

*These authors are contributed equally to this work.
[a)]Authors to whom correspondence should be addressed. Electronic mails: desco@hggm.es, mabella@ing.uc3m.es; Telephones: 916248194, 915868824.

REFERENCES

1. Rosety-Rodríguez M, Fornieles G, Rosety I, et al. Central obesity measurements predict metabolic syndrome in a retrospective cohort study of postmenopausal women. *Nutr Hosp*. 2013;28:1912–1917.
2. Sievänen H, Kannus P, Oja P, Vuori I. Precision of dual energy x-ray absorptiometry in the upper extremities. *Bone Mineral*. 1993;20:235–243.
3. Lai KC, Goodsitt MM, Murano R, Chesnut CH. A comparison of two dual-energy x-ray absorptiometry systems for spinal bone mineral measurement. *Calcif Tissue Int*. 1992;50:203–208.
4. Shkumat N, Siewerdsen J, Dhanantwari A, et al. Optimization of image acquisition techniques for dual-energy imaging of the chest. *Med Phys*. 2007;34:3904–3915.
5. Ergun DL, Mistretta CA, Brown DE, et al. Single-exposure dual-energy computed radiography: improved detection and processing. *Radiology*. 1990;174:243–249.
6. Sabol JM, Avinash GB, Nicolas F, Claus BE, Zhao J, Dobbins JT III.Development and characterization of a dual-energy subtraction imaging system for chest radiography based on CsI: Tl amorphous silicon flat-panel technology. Paper presented at: Medical Imaging 2001: Physics of Medical Imaging 2001.
7. Jabri KN, Avinash GB, Sabol JM, Nicolas FS, Uppaluri R, Hamadeh MA. Automatic selection of the log-subtraction decomposition parameters for dual energy chest radiography. Google Patents; 2006.
8. Bertens T. Calibration free dual energy radiography method. Google Patents;2016.
9. Lehmann L, Alvarez R, Macovski A, et al. Generalized image combinations in dual KVP digital radiography. *Med Phys*. 1981;8:659–667.
10. Heinzerling J, Schlindwein M. Non-linear techniques in multi-spectral x-ray imaging. *IEEE Trans Nucl Sci*. 1980;27:961–968.
11. Chuang K-S, Huang H. Comparison of four dual energy image decomposition methods. *Phys Med Biol*. 1988;33:455.
12. Lee M, Lee D, Kim H, Choi S, Kim D, Kim H-J. Development of a nonlinear dual-energy technique in chest radiography. *Radiat Phys Chem*. 2020:108811.
13. Gingold EL, Hasegawa BH. Systematic bias in basis material decomposition applied to quantitative dual-energy x-ray imaging. *Med Phys*. 1992;19:25–33.
14. Alvarez RE, Macovski A. Energy-selective reconstructions in x-ray computerised tomography. *Phys Med Biol*. 1976;21:733.
15. Brody WR, Butt G, Hall A, Macovski A. A method for selective tissue and bone visualization using dual energy scanned projection radiography. *Med Phys*. 1981;8:353–357.
16. Lim Y, Kim G, Park C, et al. Implementation of the weighted l1-norm scatter correction scheme in dual-energy radiography. *J Korean Phys Soc*. 2019;74:414–420.
17. Kappadath SC, Shaw CC. Dual-energy digital mammography: Calibration and inverse-mapping techniques to estimate calcification thickness and glandular-tissue ratio. *Med Phys*. 2003;30:1110–1117.
18. Cardinal HN, Fenster A. An accurate method for direct dual-energy calibration and decomposition. *Med Phys*. 1990;17:327–341.
19. Abella M, Serrano E, Garcia- Blas J, et al. FUX-Sim: implementation of a fast universal simulation/reconstruction framework for x-ray systems. *PLoS One*. 2017;12:e0180363.
20. Siewerdsen J, Waese A, Moseley D, Richard S, Jaffray D. Spektr: a computational tool for x-ray spectral analysis and imaging system optimization. *Med Phys*. 2004;31:3057–3067.
21. Hubbell JH, Seltzer SM. Tables of X-ray mass attenuation coefficients and mass energy-absorption coefficients 1 keV to 20 MeV for elements

Z= 1 to 92 and 48 additional substances of dosimetric interest. National Inst. of Standards and Technology-PL, Gaithersburg, MD (United States). Ionizing Radiation Div. 1995.
22. White DR, Booz J, Griffith RV, Spokas JJ, Wilson IJ. Tissue substitutes in radiation dosimetry and measurement (Report 44). *J Int Commiss Radiat Units Measur*. 2016;os23:NP.
23. Diederich S, Wormanns D. Impact of low-dose CT on lung cancer screening. *Lung Cancer*. 2004;45:S13–S19.
24. Sugerman H, Windsor A, Bessos M, Wolfe L. Intra-abdominal pressure, sagittal abdominal diameter and obesity comorbidity. *J Intern Med*. 1997;241:71–79.
25. Braby L, Johnson G, Barthe J. Practical considerations in the design and construction of tissue-equivalent proportional counters. *Radiat Prot Dosimetry*. 1995;61:351–379.
26. Collums TL. Comparison of plastics used in tissue equivalent proportional counters (TEPC) and development of a balloon borne TEPC. Oklahoma State University; 2012.
27. Hasegawa BH, Lang TF, Brown JK, et al. Object-specific attenuation correction of SPECT with correlated dual-energy x-ray CT. *IEEE Trans Nucl Sci*. 1993;40:1242–1252.
28. Goodsitt MM. Evaluation of a new set of calibration standards for the measurement of fat content via DPA and DXA. *Med Phys*. 1992;19:35–44.
29. White D, Martin R, Darlison R. Epoxy resin based tissue substitutes. *Br J Radiol*. 1977;50:814–821.
30. Jones AK, Hintenlang D, Bolch W. Tissue-equivalent materials for construction of tomographic dosimetry phantoms in pediatric radiology. *Med Phys*. 2003;30:2072–2081.
31. Kuhlman JE, Collins J, Brooks GN, Yandow DR, Broderick LS. Dual-energy subtraction chest radiography: what to look for beyond calcified nodules. *Radiographics*. 2006;26:79–92.
32. FitzGerald PF, Colborn RE, Edic PM, Lambert JW, Bonitatibus PJ, Yeh BM. Liquid tissue surrogates for X-ray and CT phantom studies. *Med Phys*. 2017;44:6251–6260.